mathematics

Article

The Shape Entropy of Small Bodies

Yanshuo Ni [1,*], He Zhang [1], Junfeng Li [2], Hexi Baoyin [2] and Jiaye Hu [3]

1 Beijing Institute of Spacecraft System Engineering, Beijing 100094, China
2 School of Aerospace Engineering, Tsinghua University, Beijing 100084, China
3 Aerospace Engineering Consulting (Beijing) Co., Ltd., China Aerospace Academy of Systems Science and Engineering, Beijing 100048, China
* Correspondence: niyanshuo007@163.com

Abstract: The irregular shapes of small bodies usually lead to non-uniform distributions of mass, which makes dynamic behaviors in the vicinities of small bodies different to that of planets. This study proposes shape entropy (SE) as an index that compares the shapes of small bodies and spheres to describe the shape of a small body. The results of derivation and calculation of SE in two-dimensional and three-dimensional cases show that: SE is independent of the size of geometric figures but depends on the shape of the figures; the SE difference between a geometric figure and a circle or a sphere, which is the limit of SE value, reflects the difference between this figure and a circle or a sphere. Therefore, the description of shapes of small bodies, such as near-spherical, ellipsoid, and elongated, can be quantitatively described via a continuous index. Combining SE and the original inertia index, describing the shape of small bodies, can define the shapes of small bodies and provide a reasonably simple metric to describe a complex shape that is applicable to generalized discussion and analysis rather than highly detailed work on a specific, unique, polyhedral model.

Keywords: entropy; applied mathematics; mathematical physics; small body

MSC: 70F15; 37M25

check for updates

Citation: Ni, Y.; Zhang, H.; Li, J.; Baoyin, H.; Hu, J. The Shape Entropy of Small Bodies. *Mathematics* **2023**, *11*, 878. https://doi.org/10.3390/math11040878

Academic Editors: Gabriel Eduard Vilcu and Jean-Charles Pinoli

Received: 17 December 2022
Revised: 4 February 2023
Accepted: 7 February 2023
Published: 9 February 2023

1. Introduction

Small Solar System Bodies (hereafter called small bodies) offer unique opportunities to study the mechanical structures, different processes, and responses that are related to the origin, evolution, and current architecture of the Solar System [1]. Small bodies are all other objects orbiting the Sun that are neither planets, dwarf planets, nor satellites, according to International Astronomical Union (IAU) resolutions five and six (Resolution_GA26-5-6) [2,3]. Therefore, a small body lacks sufficient mass for its self-gravity to overcome rigid body forces and assume hydrostatic equilibrium in a nearly round shape [2], which leads to irregular shapes of small bodies.

The shapes of small bodies span from spherical to ellipsoidal and elongated [4]. It is the irregular distribution of mass in space, caused by irregular shapes, that makes the dynamic characteristics of small bodies, such as equilibrium points [5–7] and periodic orbits [8–13], different from that of planets, provides rich research contents for celestial mechanics and nonlinear dynamics, and brings challenges to the orbit design and control of spacecraft in the vicinity of small bodies. Besides, fly-by, impacting, and rendezvous missions to small bodies demand that the shape of small bodies is accurately known to select the best-suited image processing technique for optical navigation, such as the center of brightness, intensity weighted centroiding, correlation with Lambertian spheres, and center finding by correlation [14,15]. However, this information may not always be available from ground-based observation for interplanetary missions. Spacecraft should be able to return good navigation results with the proper technique according to the shape, though small bodies can assume a wide variety of shapes.

Although the shape regularity of a small body significantly impacts the dynamical characteristics of its gravitational field and the robustness of the image processing for optical navigation, there is a lack of sufficient description, research, and quantitative analysis on the regularity of a small body, simulated by a polyhedral model with a single parameter, for further understanding on the dynamic behavior related to shapes of small bodies. Hu and Scheeres [16] defined an index describing the shape of a small body according to its principal moments of inertia, which is developed from Scheeres et al. [17]

$$\rho = \frac{I_y - I_x}{I_z - I_x}, \tag{1}$$

where the z-axis is the principal axis with maximum inertia, and the x-axis is with minimum inertia, i.e., $I_x \leq I_y \leq I_z$. According to Equation (1), the index is $\rho \in [0, 1]$. When $\rho = 0$, the shape of the small body is symmetric about the z-axis; when $\rho = 1$, the shape is symmetric about the x-axis. This shape index can describe the mass distribution characteristics of small bodies and reflect the shape of small bodies to a certain extent. However, when the shape of a small body is close to a sphere, that is, the three-axis inertias are very close, this index cannot accurately describe the shape characteristics of a small body, especially the approximation between the small body and the sphere.

Although it is possible to describe the regularity of the shape of a small body by spherical harmonic coefficients, the similarity between the shape of the small body and the sphere can only be accurately described by the multi-dimensional array composed of many spherical harmonic coefficients, which is not conducive to directly judging the shape similarity of different small bodies through a few indicators. If we investigate the coefficients C_{20}, C_{22}, and S_{22} [18], we can find that these three coefficients still reflect the relationship between the inertia of small bodies.

Approximating a small body to a triaxial ellipsoid [19,20] is also possible to describe the regularity of the shape of a small body; however, the gravitational field in the vicinity of a triaxial ellipsoid is different from that of the small body, and the dynamical characteristics in the triaxial ellipsoid case [20] is thus distinct from the polyhedron case [21], which is more accurate.

Jiang et al. [22] reviewed the common approximate models of gravitational fields, such as the simple geometry models [23–27], the spherical harmonic and ellipsoidal harmonic function model [28–33], the particle group model [34], and the polyhedral model [35–38]. In the studies of dynamic characteristics, the accuracy of the description of the gravitational field near irregular small bodies and the collision test is much more of a concern. Therefore, it is more reasonable to select the polyhedral model as the gravitational field model of the particle motion near an irregular small body [39–42].

Buonagura et al. [43] developed a shape-cube method to describe the shapes of small bodies from regular to irregular. Fifteen small bodies were placed into three layers according to whether they were near-spherical bodies, approximated to ellipsoids, or elongated and irregular bodies. In this shape-cube method, shapes of small bodies can be described as linear combinations of the starting ones. However, there is still a lack of a continuous index to quantitatively describe which small bodies should be recognized as near-spherical bodies, approximated to ellipsoids, or elongated bodies. Since Buonagura et al. used this method to assess the image processing robustness of small-body shapes and to compare the best technique, it would be better to have an index to define layers.

In this research, with the concept of entropy in statistical physics, a characteristic shape index, called shape entropy, is proposed to compare the shape difference between small bodies and uniform spheres. Entropy mainly describes the degree of data concentration, which differs from the variance as entropy has more tremendous advantages in describing the degree of data concentration with a multimodal distribution. When the data set distributes near several peaks, the variance will reflect that the data is not centralized enough, while the entropy can still reflect the data set with obvious peaks. Ni et al. have given a detailed description and derivation [44].

In order to illustrate the applicability of shape entropy, firstly, in Section 2, the shape differences among regular polygons, rectangles, ellipses, and circles with different aspect ratios are compared by using shape entropy using the 2D continuous case. Secondly, in Section 3, the shape differences among three kinds of regular polyhedrons, cuboids, triaxial ellipsoids with different axial length ratios, and spheres are compared by using shape entropy using the 3D continuous case. Finally, in Section 4, combined with the characteristics of the polyhedral models, the shape entropies are used to describe the shape differences between the small bodies and the homogeneous spheres of equal volume in the cases of three-dimensional discretization, and the results are compared with that of Equation (1).

2. Shape Entropy in the 2D Continuous Cases

2.1. Definition

A plane geometric figure is compared with a circle. According to the polar coordinates defined in Figure 1, we have a normalized quantity

$$p_s(\theta) = \frac{r_s(\theta)^2/2}{\int_0^{2\pi}(r_s(\theta)^2/2)\mathrm{d}\theta}, \tag{2}$$

where $r_s(\theta)$ is a single-valued function, and the denominator part depicts the area of the plane geometry, making

$$\int_0^{2\pi} p_s \mathrm{d}\theta = 1. \tag{3}$$

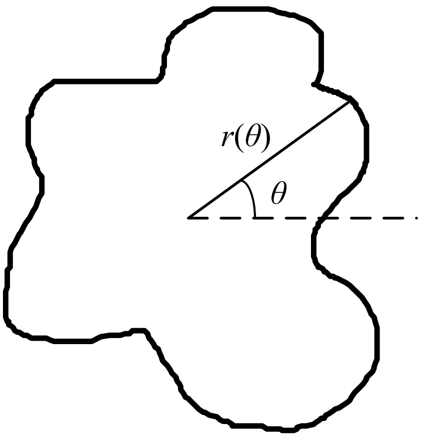

Figure 1. An illustration of arbitrary planar geometry.

The shape entropy in the 2D continuous case is defined as

$$S = -\int_0^{2\pi} p_s \log(p_s)\mathrm{d}\theta. \tag{4}$$

For a circle with radius a, we have $r_s(\theta) \equiv a$, thus

$$p_s(\theta) = \frac{r_s(\theta)^2/2}{\int_0^{2\pi}(r_s(\theta)^2/2)\mathrm{d}\theta} = \frac{a^2/2}{\pi a^2} = \frac{1}{2\pi}, \tag{5}$$

$$S = -\int_0^{2\pi} p_s \log(p_s)\mathrm{d}\theta = \log(2\pi) = 1.83788\ldots \tag{6}$$

2.2. Regular Polygons

The shape entropies of regular polygons are calculated and compared with the result of Equation (6). The calculation diagram is illustrated in Figure 2.

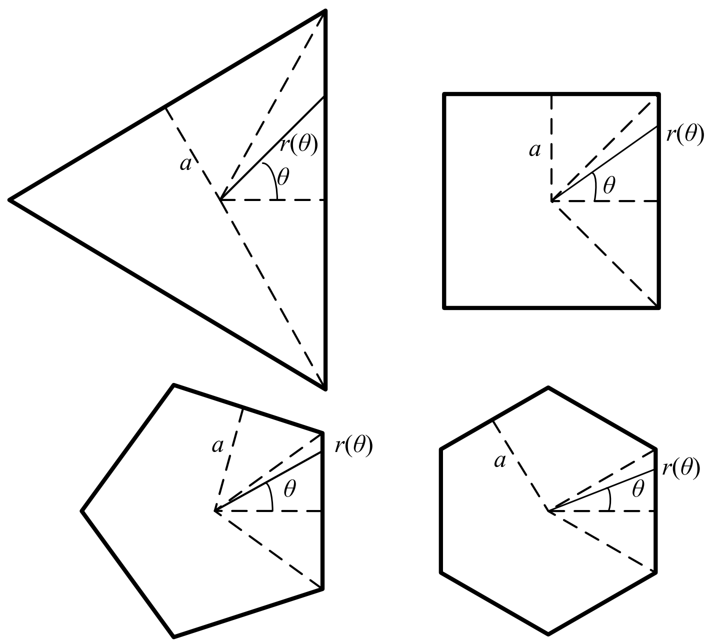

Figure 2. An illustration of regular polygon shape entropy calculations.

For a regular triangle with an inscribed circle radius a, we have

$$r_s(\theta) = \frac{a}{\cos\theta}, \theta \in \left[-\frac{\pi}{3}, \frac{\pi}{3}\right], \tag{7}$$

$$p_s(\theta) = \frac{r_s(\theta)^2/2}{3\int_{-\frac{\pi}{3}}^{\frac{\pi}{3}} (r_s(\theta)^2/2)\mathrm{d}\theta} = \frac{\frac{a^2}{2\cos^2\theta}}{6\sqrt{3}a^2} = \frac{1}{12\sqrt{3}\cos^2\theta}, \tag{8}$$

$$S = -3\int_{-\frac{\pi}{3}}^{\frac{\pi}{3}} p_s \log(p_s)\mathrm{d}\theta = 1.74557\ldots \tag{9}$$

The derivation of their entropies can be referred to as Appendix A for the square, regular pentagon, and regular hexagon cases. The results are summarized in Table 1.

Table 1. The shape entropies of regular polygons.

Number of Sides of Regular Polygons	**Shape Entropy** S
3	1.74557 …
4	1.81549 …
5	1.82964 …
6	1.83412 …
…	…
∞	$\log(2\pi) = 1.83788\ldots$

It is not difficult to see that the shape entropy is independent of the size of the geometry, a, and only related to the shape. With the increase of the regular n-sided shape, n, the value of S tends to be closer to the circular case log(2π) = 1.83788 . . . In fact, it can be obtained through calculation

$$\begin{aligned}&\lim_{n\to+\infty}-n\int_{-\frac{\pi}{n}}^{\frac{\pi}{n}}\frac{\frac{a^2}{2\cos^2\theta}}{n\int_{-\frac{\pi}{n}}^{\frac{\pi}{n}}\left[\frac{a^2}{2\cos^2\theta}\right]\mathrm{d}\theta}\log\left\{\frac{\frac{a^2}{2\cos^2\theta}}{n\int_{-\frac{\pi}{n}}^{\frac{\pi}{n}}\left[\frac{a^2}{2\cos^2\theta}\right]\mathrm{d}\theta}\right\}\mathrm{d}\theta\\ =&\lim_{n\to+\infty}-n\int_{-\frac{\pi}{n}}^{\frac{\pi}{n}}\left\{\frac{\sec^2\theta}{n\int_{-\frac{\pi}{n}}^{\frac{\pi}{n}}\sec^2\theta\mathrm{d}\theta}\log\left[\frac{\sec^2\theta}{n\int_{-\frac{\pi}{n}}^{\frac{\pi}{n}}\sec^2\theta\mathrm{d}\theta}\right]\right\}\mathrm{d}\theta=\log(2\pi),\end{aligned} \tag{10}$$

so that the series of shape entropy of the regular n-sided shape $\{S_n\}$ tends to the shape entropy of a circle log(2π) = 1.83788 . . . when n tends to +∞. Note that entropy in statistical physics describes the concentration of states, and the value of entropy is the largest when the probabilities of all states are equal. Thus, when r_s are equal, corresponding to the most regular case, the shape entropy in 2D cases is the largest.

2.3. Rectangles and Ellipses

For a rectangle with a long side 2a and a short side 2b, Equations (2)–(4) are transformed as

$$r_s(\theta)=\begin{cases}\frac{a}{\cos\theta},\theta\in[0,\arctan(b/a)]\\ \frac{b}{\sin\theta},\theta\in\left[\arctan(b/a),\frac{\pi}{2}\right]\end{cases}, \tag{11}$$

$$p_s(\theta)=\frac{r_s(\theta)^2/2}{4\int_0^{\frac{\pi}{2}}(r_s(\theta)^2/2)\mathrm{d}\theta}=\begin{cases}\frac{a}{8b\cos^2\theta},\theta\in[0,\arctan(b/a)]\\ \frac{b}{8a\sin^2\theta},\theta\in\left[\arctan(b/a),\frac{\pi}{2}\right]\end{cases}, \tag{12}$$

$$S=-4\int_0^{\frac{\pi}{2}}p_s\log(p_s)\mathrm{d}\theta. \tag{13}$$

The shape entropy of any rectangle can be calculated via Equations (11)–(13).

For an ellipse with a major axis 2a and a minor axis 2b, Equations (2)–(4) are transformed as

$$r_s(\theta)=\frac{ab}{\sqrt{b^2\cos^2\theta+a^2\sin^2\theta}}, \tag{14}$$

$$p_s(\theta)=\frac{r_s(\theta)^2/2}{\int_0^{\pi}(r_s(\theta)^2/2)\mathrm{d}\theta}=\frac{ab}{2\pi\left[b^2\cos^2\theta+a^2\sin^2\theta\right]}, \tag{15}$$

$$S=-\int_0^{2\pi}p_s\log(p_s)\mathrm{d}\theta. \tag{16}$$

It should be noted that Equation (14) is not the parametric equation of an ellipse.

The shape entropy of any ellipse can be calculated via Equations (14)–(16).

For different shapes of rectangles and ellipses represented by a:b, their shape entropies are calculated and summarized as Table 2.

For rectangles, when a:b tends to 1:1, S tends to the shape entropy of the square 1.81549... and when a:b = 1:1, Equations (11)–(13) degenerate to the square case Equations (A1)–(A3). The shape entropy of a rectangle is independent of the size of the rectangle and only depends on its shape, which is consistent with the general understanding.

For ellipses, when a:b tends to 1:1, S tends to the shape entropy of the circle 1.83788 . . . and when a:b = 1:1, Equations (14)–(16) degenerate to the circle case Equations (5) and (6). Similarly, as in the rectangles cases, the shape entropy of an ellipse is independent of the size and only depends on its shape, which is also consistent with the general understanding.

Comparing the results of Table 2, it can also be found that when a rectangle and an ellipse with the same length ratio are compared, the shape of the ellipse is closer to the circle, which is also consistent with general cognition.

Table 2. The shape entropies of rectangles and ellipses.

a:b	Rectangle	Ellipse
3:1	1.49387 ...	1.55019 ...
2:1	1.68228 ...	1.72009 ...
1.5:1	1.76905 ...	1.79706 ...
1:1	1.81549...	log(2π) = 1.83788 ...

For non-convex shapes described in Figure 3, Equations (11) and (12) are transformed as

$$r_s(\theta) = \begin{cases} \frac{a}{\cos\theta}, & \theta \in [0, \arctan(b/a)] \\ \sqrt{x^2(\theta) + y^2(\theta)}, & \theta \in \left[\arctan(b/a), \frac{\pi}{2}\right] \\ \text{where } x(\theta) = \frac{ac}{c-b+a\tan\theta}, y(\theta) = x(\theta)\tan\theta \end{cases}, \tag{17}$$

$$p_s(\theta) = \frac{r_s(\theta)^2/2}{4\int_0^{\frac{\pi}{2}} (r_s(\theta)^2/2)\mathrm{d}\theta} = \begin{cases} \frac{a^2}{2\cos^2\theta[4ab-2a(b-c)]}, \theta \in [0, \arctan(b/a)] \\ \frac{x^2(\theta)+y^2(\theta)}{2[4ab-2a(b-c)]}, \theta \in \left[\arctan(b/a), \frac{\pi}{2}\right] \end{cases}. \tag{18}$$

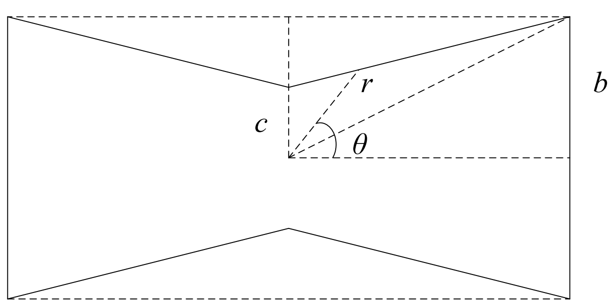

Figure 3. An illustration of the non-convex shapes transformed from a rectangle.

The shape entropies of non-convex shapes from Figure 3 are calculated as Equations (13), (17) and (18). Setting $b = 1$, c varying from 0.1 to 1 and $a = 1, 1.5, \sqrt{3}$, and 2, the shape entropies are shown in Figure 4. The results show that non-convex shapes are more irregular as c decreases, which is intuitive. Therefore, it is reasonable to compare the difference between the two-dimensional shape and the circle with the shape entropy defined by Equations (2)–(4).

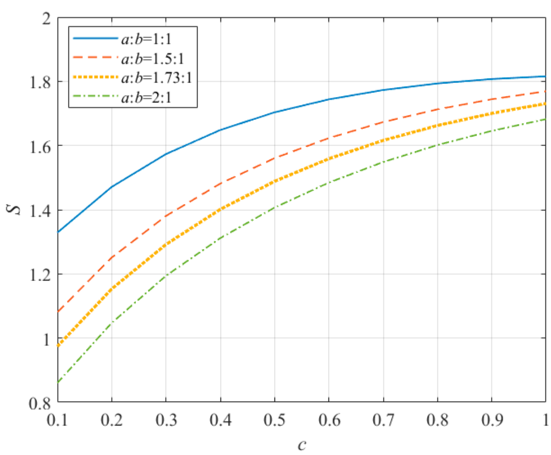

Figure 4. The shape entropies of non-convex shapes are shown in Figure 3, provided that $b = 1$, $a = 1$, 1.5, $\sqrt{3}$, 2, and $c \in [0.1, 1]$.

3. Shape Entropy in the 3D Continuous Cases

3.1. Definition

In this section, the description of the shape entropy is extended from 2D to 3D to compare the difference between spatial geometry and a sphere. According to the spherical coordinates defined in Figure 5, we can write a similar normalized quantity as in Section 2.

$$p_s(\theta,\phi) = \frac{\sin\phi\, r_s(\theta,\phi)^3/3}{\int_0^{2\pi}\int_0^{\pi}\left(r_s(\theta,\phi)^3/3\right)\sin\phi \mathrm{d}\phi\mathrm{d}\theta}, \tag{19}$$

where $r_s(\theta, \phi)$ is a single-valued function, and the denominator part depicts the volume of the spatial geometry, making

$$\int_0^{2\pi}\int_0^{\pi} p_s(\theta,\phi)\mathrm{d}\phi\mathrm{d}\theta = 1. \tag{20}$$

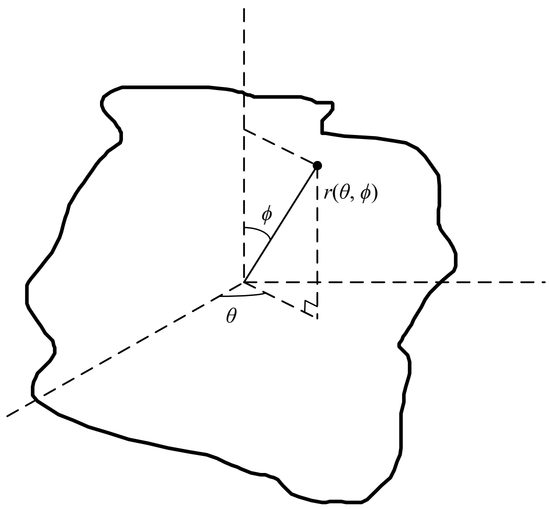

Figure 5. An illustration of arbitrary spatial geometry.

The shape entropy in the 3D continuous case is defined as

$$S = -\int_0^{2\pi}\int_0^{\pi} p_s(\theta,\phi)\log[p_s(\theta,\phi)]\mathrm{d}\phi\mathrm{d}\theta. \tag{21}$$

For a sphere with $r_s(\theta, \varphi) \equiv a$, Equation (19) is transformed as

$$p_s(\theta,\phi) = \frac{\sin\phi\, r_s(\theta,\phi)^3/3}{\int_0^{2\pi}\int_0^{\pi}\left(r_s(\theta,\phi)^3/3\right)\sin\phi \mathrm{d}\phi\mathrm{d}\theta} = \frac{\sin\phi\, a^3/3}{4\pi a^3/3} = \frac{\sin\phi}{4\pi}, \tag{22}$$

and the shape entropy calculated via Equation (21) is

$$S = -\int_0^{2\pi}\int_0^{\pi} p_s(\theta,\phi)\log[p_s(\theta,\phi)]\mathrm{d}\phi\mathrm{d}\theta = \log(2\pi) + 1 = 2.83788\ldots \tag{23}$$

3.2. Regular Polyhedrons

In this subsection, the shape entropies of a regular tetrahedron, hexahedron, and octahedron are derived and summarized in Table 3. For a regular tetrahedron, 1/24 of it is taken according to symmetry, as shown in Figure 6, and it can be deduced that:

$$r_s(\theta,\phi) = \frac{a}{\cos\phi}, \theta \in \left[0, \frac{\pi}{3}\right], \phi \in \left[0, \arctan\left(\frac{\sqrt{2}}{\cos\theta}\right)\right], \tag{24}$$

$$\begin{aligned} p_s(\theta,\phi) &= \frac{\sin\phi r_s(\theta,\phi)^3/3}{24\int_0^{\frac{\pi}{3}}\int_0^{\arctan[\frac{\sqrt{2}}{\cos\theta}]}\left(r_s(\theta,\phi)^3/3\right)\sin\phi \mathrm{d}\phi\mathrm{d}\theta} \\ &= \frac{\sin\phi a^3/3/\cos^3\phi}{8\sqrt{3}a^3} = \frac{\sin\phi}{24\sqrt{3}\cos^3\phi}, \end{aligned} \tag{25}$$

$$S = -24\int_0^{\frac{\pi}{3}}\int_0^{\arctan[\frac{\sqrt{2}}{\cos\theta}]} p_s(\theta,\phi)\log[p_s(\theta,\phi)]\mathrm{d}\phi\mathrm{d}\theta = 2.60889\ldots \tag{26}$$

Table 3. The shape entropies of regular polyhedrons.

Number of Faces of Regular Polyhedrons	Shape Entropy S
4	2.60889 ...
6	2.73379 ...
8	2.82407...
Spherical case	log(2π) + 1 = 2.83788...

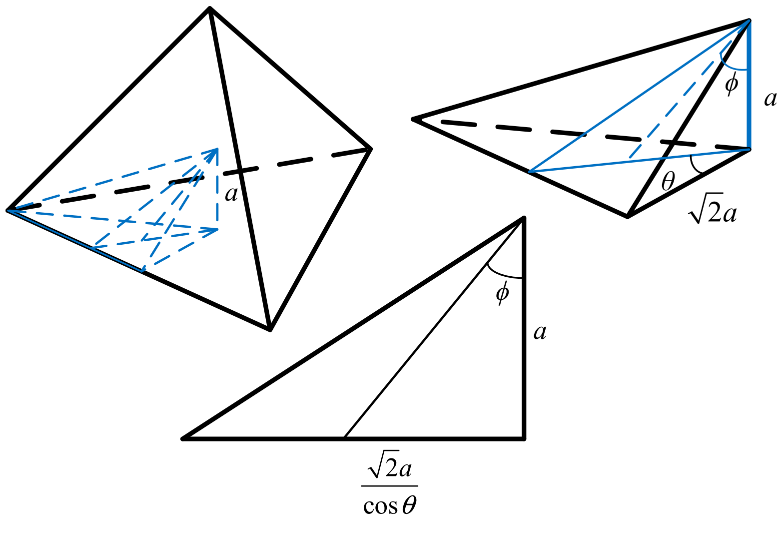

Figure 6. An illustration of a regular tetrahedron and the calculation of its shape entropy.

For a regular hexahedron with an edge length of $2a$, as shown in Figure 7, one-eighth of the hexahedron is taken according to symmetry. In this part, the distance from the point on the surface to the centroid of the regular hexahedron can be determined according to θ and φ into four parts:

$$r_s(\theta,\phi) = \begin{cases} \frac{a}{\cos\phi}, & \theta \in \left[0, \frac{\pi}{4}\right], \phi \in [0, \arctan(\cos\theta)] \\ \frac{a}{\cos\theta\sin\phi}, & \theta \in \left[0, \frac{\pi}{4}\right], \phi \in \left[\arctan(\cos\theta), \frac{\pi}{2}\right] \\ \frac{a}{\cos\phi}, & \theta \in \left[\frac{\pi}{4}, \frac{\pi}{2}\right], \phi \in [0, \arctan(\sin\theta)] \\ \frac{a}{\sin\theta\sin\phi}, & \theta \in \left[\frac{\pi}{4}, \frac{\pi}{2}\right], \phi \in \left[\arctan(\sin\theta), \frac{\pi}{2}\right] \end{cases}, \tag{27}$$

then we have

$$p_s(\theta,\phi) = \frac{{r_s}^3(\theta,\phi)\sin\phi}{24a^3}, \tag{28}$$

$$S = -8\int_0^{\frac{\pi}{2}}\int_0^{\frac{\pi}{2}} p_s(\theta,\phi)\log[p_s(\theta,\phi)]\mathrm{d}\phi\mathrm{d}\theta = 2.73379\ldots \tag{29}$$

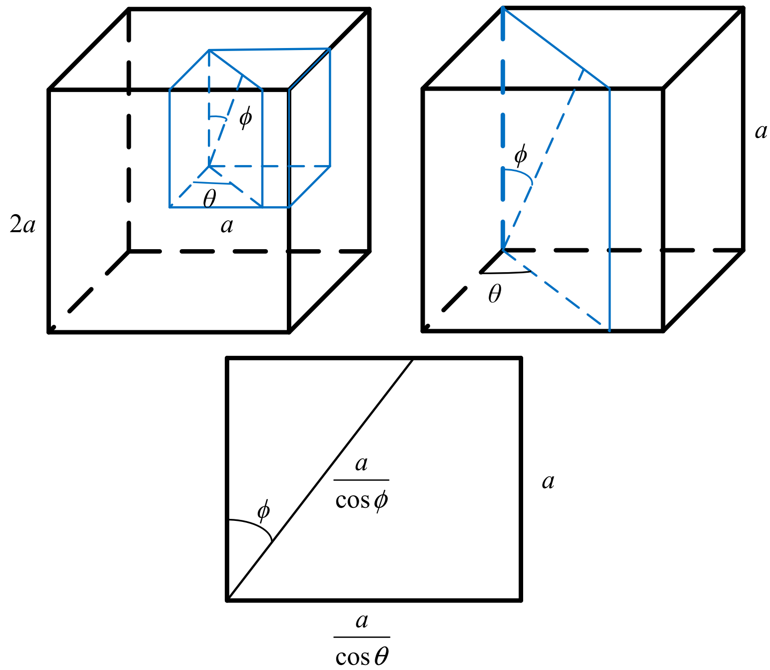

Figure 7. An illustration of a regular hexahedron and the calculation of its shape entropy.

For a regular octahedron with an edge length of 2a, as shown in Figure 8, one-eighth of the octahedron is taken according to symmetry. In this part, using the sine theorem and cosine theorem, the distance from the point on the surface of the original regular octahedron to the centroid can be expressed as:

$$r_s(\theta,\phi) = \frac{\sqrt{2}a}{\cos\phi + \sqrt{2}\cos\theta\sin\phi}, \theta \in \left[-\frac{\pi}{4},\frac{\pi}{4}\right], \phi \in \left[0,\frac{\pi}{2}\right], \tag{30}$$

Equation (19) is transformed as

$$\begin{aligned} p_s(\theta,\phi) &= \frac{\sin\phi\ r_s(\theta,\phi)^3/3}{8\int_{-\frac{\pi}{4}}^{\frac{\pi}{4}}\int_0^{\frac{\pi}{2}}\left(r_s(\theta,\phi)^3/3\right)\sin\phi\mathrm{d}\phi\mathrm{d}\theta} \\ &= \frac{\sin\phi\ r_s(\theta,\phi)^3/3}{8\sqrt{3}a^3/3} = \frac{\sin\phi\ r_s(\theta,\phi)^3}{8\sqrt{3}a^3}, \end{aligned} \tag{31}$$

so, the shape entropy of a regular octahedron is

$$S = -8\int_{-\frac{\pi}{4}}^{\frac{\pi}{4}}\int_0^{\frac{\pi}{2}} p_s(\theta,\phi)\log[p_s(\theta,\phi)]\mathrm{d}\phi\mathrm{d}\theta = 2.82407\ldots \tag{32}$$

It is not difficult to see that the shape entropy of 3D continuous cases, defined in Section 3.1, is independent of the size of the geometry, a, and is only related to the shape. With the face increasing of regular polyhedrons, the value of S is closer to the spherical case $\log(2\pi) + 1 = 2.83788...$

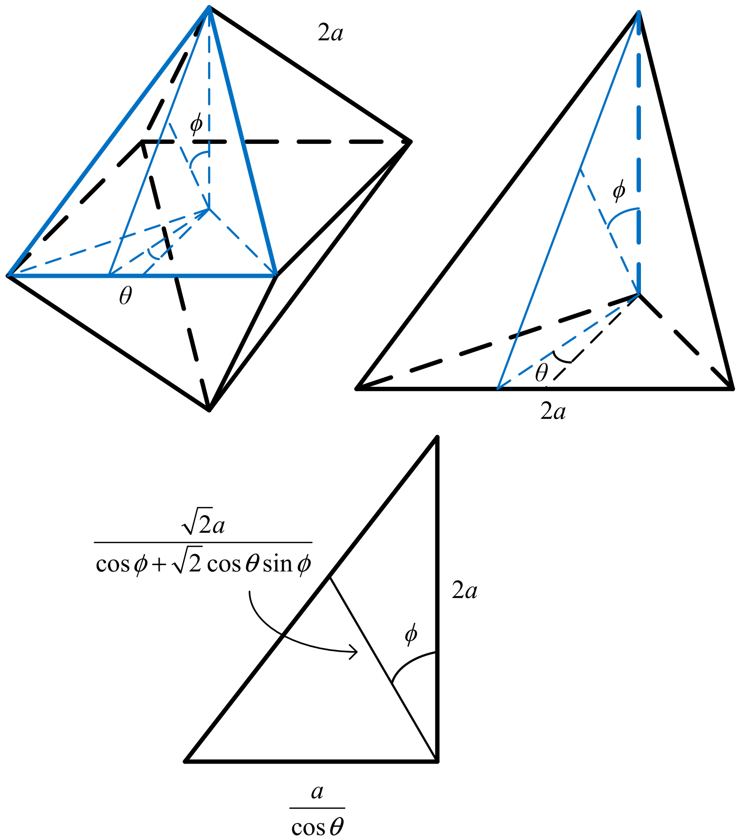

Figure 8. An illustration of a regular octahedron and the calculation of its shape entropy.

3.3. Cuboids and Triaxial Ellipsoids

For a cuboid with edge lengths $2a$, $2b$ and $2c$ respectively ($a > b > c$), it can be deduced that

$$r_s(\theta,\phi) = \begin{cases} \frac{c}{\cos\phi}, & \theta \in \left[0, \arctan\left(\frac{a}{b}\right)\right], \phi \in \left[0, \arctan\left(\frac{c}{b}\cos\theta\right)\right] \\ \frac{b}{\cos\theta\sin\phi}, & \theta \in \left[0, \arctan\left(\frac{a}{b}\right)\right], \phi \in \left[\arctan\left(\frac{c}{b}\cos\theta\right), \frac{\pi}{2}\right] \\ \frac{c}{\cos\phi}, & \theta \in \left[\arctan\left(\frac{a}{b}\right), \frac{\pi}{2}\right], \phi \in \left[0, \arctan\left(\frac{c}{a}\sin\theta\right)\right] \\ \frac{a}{\sin\theta\sin\phi}, & \theta \in \left[\arctan\left(\frac{a}{b}\right), \frac{\pi}{2}\right], \phi \in \left[\arctan\left(\frac{c}{a}\sin\theta\right), \frac{\pi}{2}\right] \end{cases}, \tag{33}$$

Equation (19) is transformed as

$$\begin{aligned} p_s(\theta,\phi) &= \frac{{r_s}^3(\theta,\phi)\sin\phi}{24abc} \\ &= \begin{cases} \frac{c^2\sin\phi}{24ab\cos^3\phi}, & \theta \in \left[0, \arctan\left(\frac{a}{b}\right)\right], \phi \in \left[0, \arctan\left(\frac{c}{b}\cos\theta\right)\right] \\ \frac{b^2}{24ac\cos^3\theta\sin^2\phi}, & \theta \in \left[0, \arctan\left(\frac{a}{b}\right)\right], \phi \in \left[\arctan\left(\frac{c}{b}\cos\theta\right), \frac{\pi}{2}\right] \\ \frac{c^2\sin\phi}{24ab\cos^3\phi}, & \theta \in \left[\arctan\left(\frac{a}{b}\right), \frac{\pi}{2}\right], \phi \in \left[0, \arctan\left(\frac{c}{a}\sin\theta\right)\right] \\ \frac{a^2}{24bc\sin^3\theta\sin^2\phi}, & \theta \in \left[\arctan\left(\frac{a}{b}\right), \frac{\pi}{2}\right], \phi \in \left[\arctan\left(\frac{c}{a}\sin\theta\right), \frac{\pi}{2}\right] \end{cases}, \end{aligned} \tag{34}$$

and the shape entropy of the cuboid is

$$S = -8\int_0^{\frac{\pi}{2}}\int_0^{\frac{\pi}{2}} p_s(\theta,\phi)\log[p_s(\theta,\phi)]\mathrm{d}\phi\mathrm{d}\theta. \tag{35}$$

The shape entropy of an arbitrary cuboid can be calculated by Equations (33)–(35). Shape entropies of cuboids with different combinations of a and b, provided that $c = 1$, are calculated, and the results are shown in Figure 9. When a:b:c = 1:1:1, Equation (33) degenerates to Equation (27), and the shape entropy equals the hexahedron case 2.73379....

It is shown again that the shape entropy of a cuboid is independent of the size, and only depends on the shape of the cuboid.

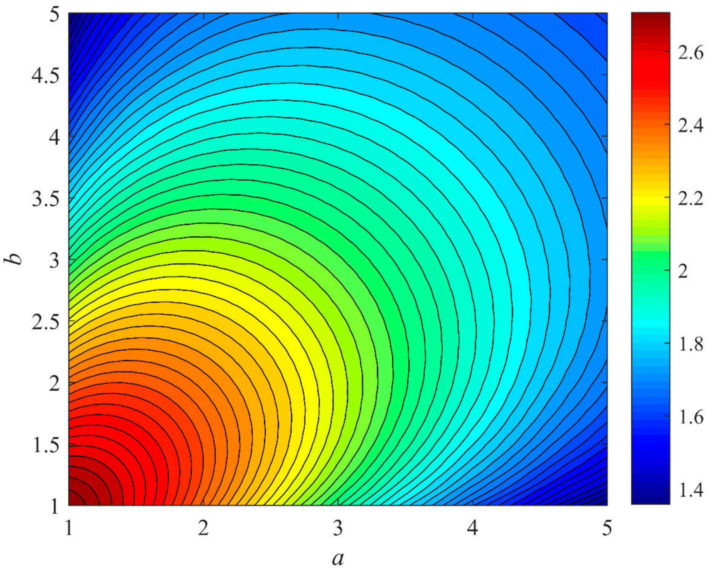

Figure 9. The shape entropies of cuboids with different edge length ratios of a and b, provided that c = 1. The blue area suggests a more irregular shape. The lower left corner corresponds to the regular hexahedron.

For an ellipsoid with triaxial lengths 2a, 2b and 2c respectively ($a > b > c$), it can be deduced that

$$r_s(\theta,\phi) = \frac{abc}{\sqrt{b^2c^2cos^2\phi\sin^2\theta + a^2c^2\sin^2\phi\sin^2\theta + a^2b^2\cos^2\phi}}, \tag{36}$$

$$\begin{aligned} p_s(\theta,\phi) &= \frac{\sin\phi\ r_s(\theta,\phi)^3/3}{\int_0^{2\pi}\int_0^{\pi}\left(r_s(\theta,\phi)^3/3\right)\sin\phi \mathrm{d}\phi\mathrm{d}\theta} \\ &= \frac{\sin\phi\ r_s(\theta,\phi)^3/3}{4\pi abc/3} = \frac{\sin\phi\ r_s(\theta,\phi)^3}{4\pi abc}, \end{aligned} \tag{37}$$

$$S = -\int_0^{2\pi}\int_0^{\pi} p_s\log(p_s)\mathrm{d}\phi\mathrm{d}\theta. \tag{38}$$

It should also be noted that Equation (36) is not the parametric equation of an ellipsoid.

The shape entropy of an arbitrary ellipsoid can be calculated by Equations (36)–(38). Shape entropies of ellipsoids with different combinations of a and b, provided that c = 1, are calculated, and results are shown in Figure 10. When a:b:c = 1:1:1, Equation (36) degenerates to the sphere case, and the shape entropy equals the sphere case. It is shown again that the shape entropy of an ellipsoid is independent of the size, and only depends on the shape of the ellipsoid.

By comparing the results of a few values of a and b, summarized in Table 4, it can also be deduced that the shape of the ellipsoid is closer to the sphere when a cuboid and an ellipsoid with the same axial/edge length ratio are compared. When c = 1, the difference between the shape entropy of the ellipsoid and the cuboid calculated by different combinations of a and b is shown in Figure 11. It can be seen that when the shape is close to slender, the difference between the shape of the ellipsoid and the cuboid is more significant; when the shape is nearly flat, the difference between the ellipsoid and the cuboid is relatively small; when the axial/edge length ratio is 1:1:1, the shape difference between the two is minimal.

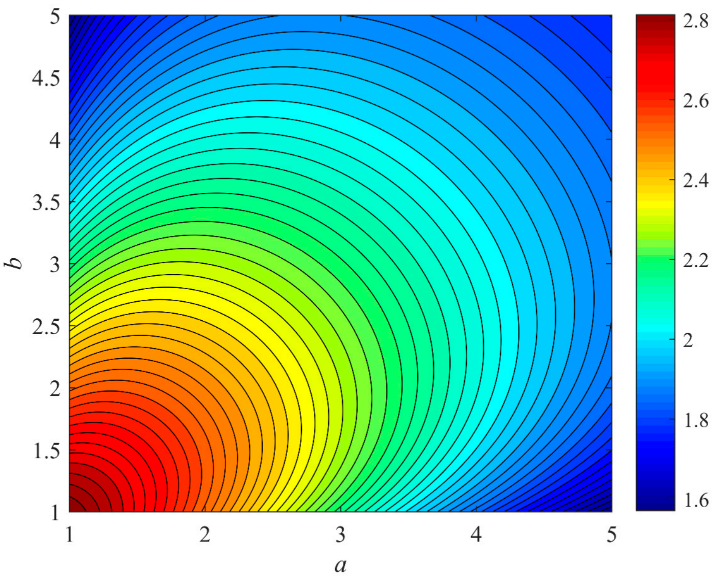

Figure 10. The shape entropies of ellipsoids with different axial length ratios of a and b, provided that $c = 1$. The blue area suggests a more irregular shape. The lower left corner corresponds to the sphere.

Table 4. The shape entropies of cuboids and ellipsoids.

a*:*b*:*c	**Cuboid**	**Ellipsoid**
3:2:1	2.15642 ...	2.29111 ...
2:2:1	2.37094 ...	2.48964 ...
2:1.5:1	2.43230 ...	2.55064 ...
1:1:1	2.73379....	$\log(2\pi) + 1 = 2.83788\ldots$

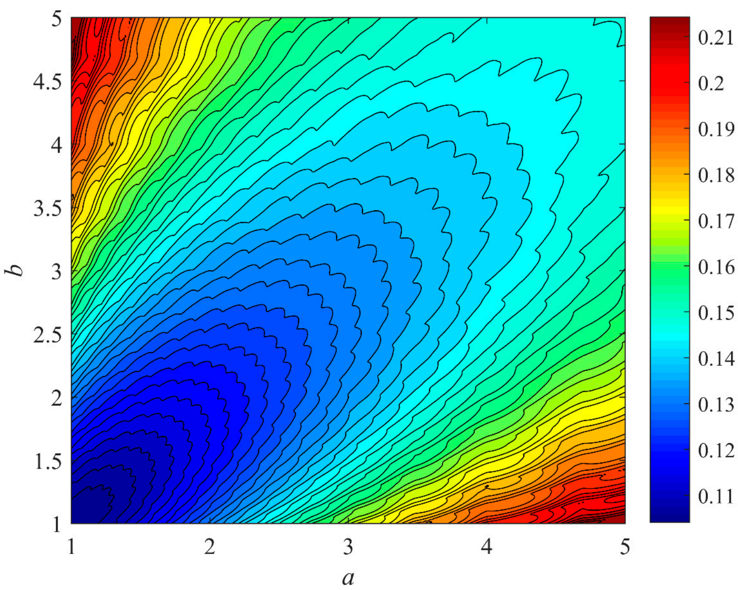

Figure 11. The differences in shape entropies of ellipsoids and cuboids with different axial length ratios. The blue area suggests less difference. Since it is assumed that $c = 1$ for all shapes shown, diagonal line $a = b$ corresponds to flat shapes, and axis a or b corresponds to slender shapes.

4. Shape Entropy Applied to Polyhedral Models of Small Bodies

4.1. Definition

Since the polyhedral models of small bodies are discrete vertex-face models, we transform Equation (19) as

$$p_S^n = \frac{r_S^n}{\sum\limits_{n=1}^{N} r_S^n}, \tag{39}$$

where r_S^n denotes the distance between the nth vertex and the centroid, and N denotes the number of vertices. Equation (39) is a normalized quantity whose denominator part is the sum of the distances from all vertices to the centroid, making

$$\sum_{n=1}^{N} p_S^n = 1. \tag{40}$$

The shape entropy of the polyhedral model of a small body is defined as

$$S = -\sum_{n=1}^{N} p_S^n \log(p_S^n) - \log(N). \tag{41}$$

At the last term of Equation (41), $\log(N)$ is subtracted to eliminate the influence caused by the different number of vertices of polyhedral models. When the object is a sphere, each point is the same distance from the centroid, and the shape entropy is

$$S = -\sum_{n=1}^{N} \frac{1}{N} \log\left(\frac{1}{N}\right) - \log(N) = log(N) - \log(N) = 0. \tag{42}$$

By comparing the shape entropy S, as defined by Equations (39)–(41), we can compare the shape of the polyhedral model with that of the homogeneous sphere with equal volume.

4.2. Results

The shape entropies, S, of some polyhedral models [45] of small bodies are calculated according to Equations (39)–(41) and are listed in Table 5 in the order of S from large to small, listed together with the values of ρ from Equation (1). It can be seen that although the shape entropies of the first four small bodies are the same, the range of ρ is extensive. It can be seen more clearly from Figure 12 that the four near-spherical small bodies, corresponding to points 1–4, are on the most right in the figure, and their shapes are close to spheres (Figure 13). Although the four small bodies approximated to ellipsoids (Figure 14), corresponding to points 5–8, have specific differences in shape and spheres, they are obviously different from the shape of elongated small bodies, corresponding to points 9–12 (Figure 15), on the left of the figure.

Only ρ calculated by Equation (1) cannot describe the shape well. When the principal moments of inertia of the small body are relatively close, the ρ values differ significantly. However, the appearances of small bodies are similar, such as the four small bodies numbered 1–4. The appearance and shape of small bodies with similar ρ values may also differ significantly, such as small bodies 6 and 8, and 9–12. The shape of the polyhedral model can be compared with that of the homogeneous sphere of the same volume sphere with the help of Equation (42), and the shape of the small body can be better described together with Equation (1).

According to the results in Table 5 and Figure 12, the shapes of small bodies from near-spherical to elongated can be described with shape entropy from large to small. The new description is quantitative rather than terms without accurate definitions, although the exact demarcation for near-spherical, ellipsoids, and elongated can be further discussed. In this work, we suggest that so-called near-spherical bodies have shape entropies larger than -0.004, small bodies approximated to ellipsoids corresponding to those whose entropies lie between −0.02 and −0.004, and small bodies with shape entropies less than −0.02 can be labeled as elongated. It would also be more applicable in a further discussion on characteristics related to shapes.

Table 5. The shape entropies of polyhedral models of small bodies.

Name of Small Bodies	Shape Entropy S	Vertices	Faces	ρ from Equation (1)	No. in Figure 12
52760 (1998 ML_{14})	−0.001118600	8162	16,320	0.877608	1
101955 Bennu	−0.001171272	1348	2692	0.320574	2
1998 KY_{26}	−0.001469927	2048	4092	0.823293	3
4 Vesta	−0.003386096	2522	5040	0.165797	4
9P/Tempel	−0.008419353	16,022	32,040	0.779807	5
6489 Golevka	−0.011491285	2048	4092	0.964472	6
3103 Eger	−0.013905315	997	1990	0.648360	7
951 Gaspra	−0.019957635	2522	5040	0.914083	8
4769 Castalia	−0.028763986	2048	4092	0.896695	/
2063 Bacchus	−0.034839183	2048	4092	0.986248	/
25143 Itokawa	−0.039069503	25,350	49,152	0.932418	/
1P/Halley	−0.039881773	2522	5040	0.934006	/
1620 Geographos	−0.042576975	8192	16,380	0.942497	/
4486 Mithra	−0.049464462	3000	5996	0.860466	/
1996 HW_1	−0.057551792	1392	2780	0.973871	/
433 Eros	−0.060992619	99,846	196,608	0.978736	9
216 Kleopatra	−0.074191101	2048	4092	0.990365	10
243 Ida	−0.085757437	2522	5040	0.883693	11
103P/Hartley	−0.098676873	16,022	32,040	0.975002	12

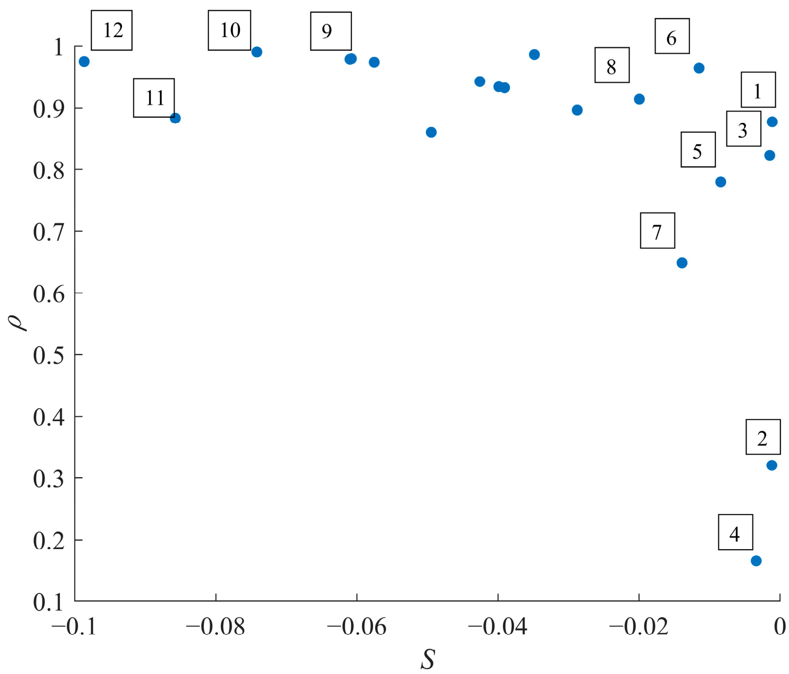

Figure 12. The distribution of shape entropies (S) and ρ from Equation (1) of different small bodies. No. 1–12 can be referred in Table 5, and their shapes are shown in Figures 13–15.

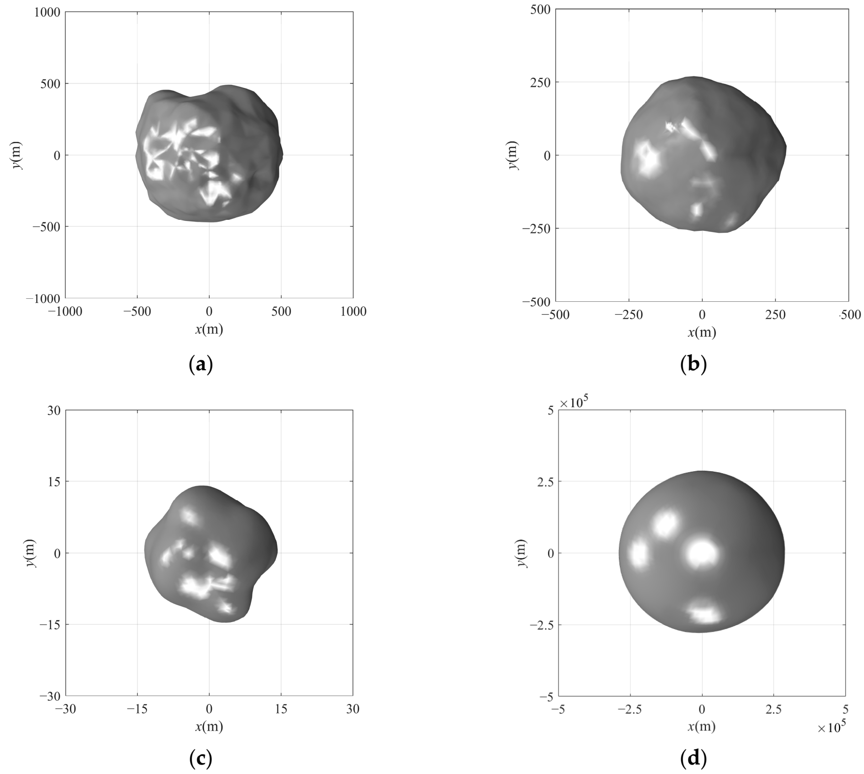

Figure 13. Polyhedral models corresponding to points 1–4 in Figure 12. (**a**) 52,760 (1998 ML_{14}). (**b**) 101,955 Bennu. (**c**) 1998 KY_{26}. (**d**) 4 Vesta.

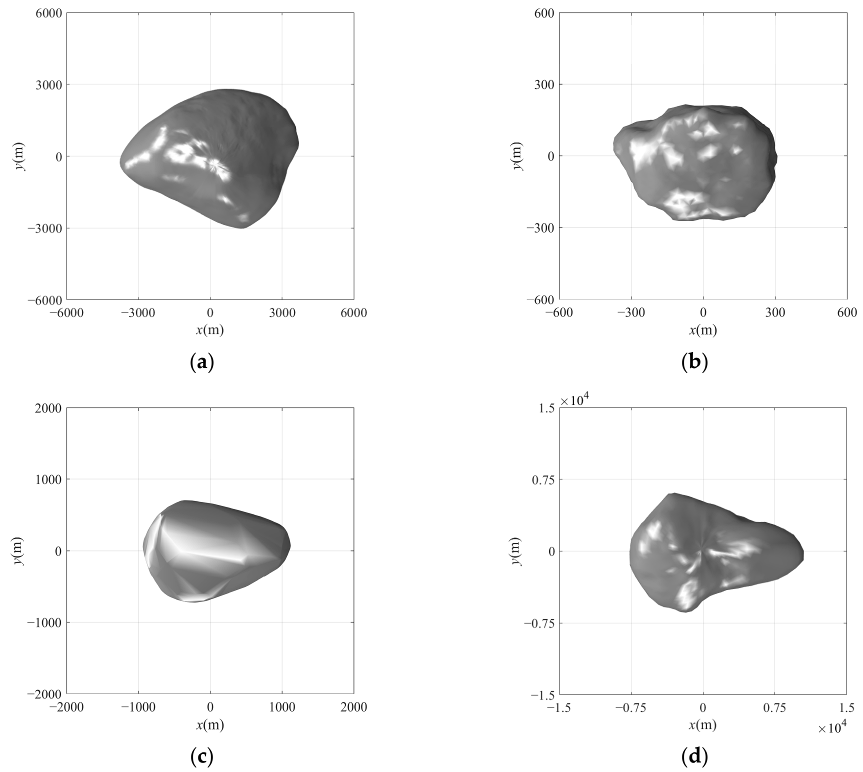

Figure 14. Polyhedral models corresponding to points 5–8 in Figure 12. (**a**) 9P/Tempel. (**b**) 6489 Golevka. (**c**) 3103 Eger. (**d**) 951 Gaspra.

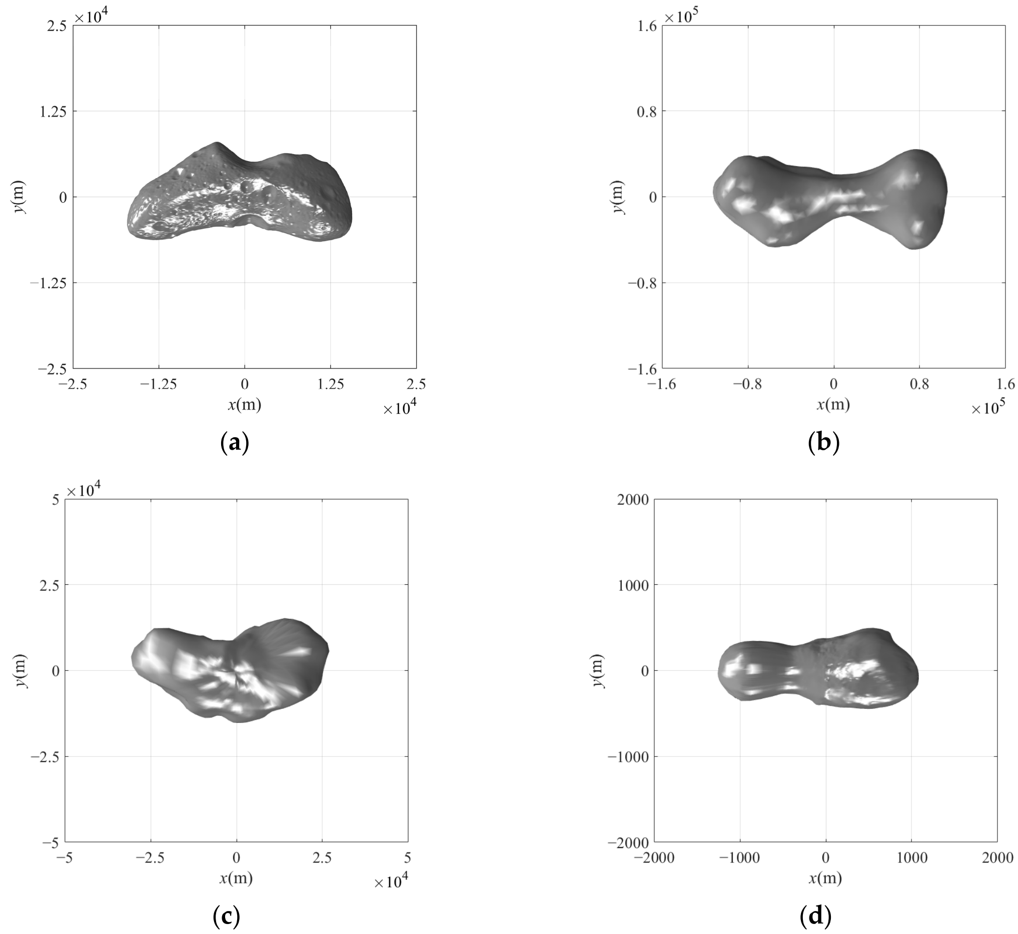

Figure 15. Polyhedral models corresponding to points 9–12 in Figure 12. (**a**) 433 Eros. (**b**) 216 Kleopatra. (**c**) 243 Ida. (**d**) 103P/Hartley.

5. Conclusions

This study proposes shape entropy as an index to compare the shape differences between small bodies and homogeneous spheres of equal volume. First, the methods of comparing plane geometry with circle and space geometry with sphere by using the shape entropy in continuous cases are given, and then the shape entropy applied to discrete cases is derived for polyhedral models. The shape entropy is independent of the size of the geometry and only depends on the shape.

In comparing plane geometric figures with circles, the shape entropies of circles and regular polygons are derived and calculated. It is proved that when n tends to infinity, the shape entropy of the regular n-sided shape tends to that of the circle. The shape entropies of rectangles and ellipses are derived and calculated, respectively. The shape entropy is used to compare the rectangle and ellipse with the same edge/axis length ratio. The shape entropies of dumbbell-like non-convex shapes transformed from rectangles are also calculated, and results show that such shapes are more irregular as their necks are more narrow, which is intuitive. Derivation and calculation prove that comparing plane geometries with circles by shape entropies is reasonable.

In comparing space geometric figures with spheres, due to the limited number of regular polyhedrons, the shape entropies of spheres, regular tetrahedrons, regular hexahedrons, and regular octahedrons are derived and calculated. It is found that the shape entropy of regular polyhedrons approaches the shape entropy of spheres with the increase in the number of faces. The shape entropies of cuboids and ellipsoids are derived and calculated, respectively. The rationality is verified by comparing different edge/axial length ratios until they degenerate to cube and sphere, respectively. The shape differences between cuboids and ellipsoids with the same edge/axial length ratio are compared by using shape entropy. The difference between an ellipsoid and a cuboid is more significant when the shape is close to slender. The difference between an ellipsoid and a cuboid is relatively small when the shape is nearly flat. When the axial/edge length ratio is 1:1:1, the shape difference between the ellipsoid and the cuboid is the smallest. Derivation and calculation prove that comparing space geometries with spheres with shape entropies is reasonable.

Sections 2 and 3 show that shape entropy is suitable for comparing 2D and 3D geometric figures with circles and spheres under continuous conditions, and the entropies of circles and spheres are the limit values in 2D and 3D cases, respectively. The difference between the shape entropy of each geometric figure and the limit value reflects the difference between this figure and the circle or sphere in shape.

A discrete form of the shape entropy is defined for small bodies simulated by polyhedral models. The shape entropies of 19 small bodies with polyhedral models are calculated, which describes the comparison results between small bodies and homogeneous spheres of equal volume. The shape comparison results between different small bodies are compared using both the shape entropy, S, and the inertia index, ρ, proposed by Hu and Scheeres [16]. For small bodies with shape entropies larger than -0.004, the inertia indices vary in the whole range of [0, 1] due to the three-axis inertia being very close; thus can not describe so-called near-spherical small bodies well. The shape entropy of a sphere body is zero, and the shape entropy of a small body decreases as the shape varies from near-spherical to elongated. The former so-called near-spherical small bodies, small bodies approximated to ellipsoids, and elongated small bodies, in Buonagura et al. [43], can be referred to as shape entropies larger than -0.004, between -0.02 and -0.004, and smaller than -0.02, respectively.

Therefore, shape entropy is a continuous index and provides a reasonably simple metric to quantitatively describe a complex shape (such as the shape of small bodies) in a generalized discussion and analysis, including further research on the shape effect of dynamic behaviors in the vicinity of small bodies (which is related to both shape/mass distribution and rotation rate and, therefore, is limited to reflect behaviors independently) and on-board optical navigations during interplanetary missions, as mentioned in the introduction, rather than highly detailed work on a specific, unique, polyhedral model.

Author Contributions: Conceptualization, Y.N. and J.L.; methodology, Y.N.; validation, H.Z., H.B. and J.L.; formal analysis, Y.N.; investigation, J.H.; data curation, Y.N.; writing—original draft preparation, Y.N. and J.H.; writing—review and editing, H.Z., J.L. and H.B.; visualization, J.H. and Y.N.; supervision, J.L. and H.B.; project administration, J.L. and H.B.; funding acquisition, H.Z. All authors have read and agreed to the published version of the manuscript.

Funding: This research is funded by the National Key R&D Program of China (grant No. 2020YFE0202100).

Institutional Review Board Statement: Not applicable.

Informed Consent Statement: Not applicable.

Data Availability Statement: All data generated or analyzed during this study are included in this published article as equations, figures, and tables.

Conflicts of Interest: The authors declare no conflict of interest.

Appendix A

For a square with an inscribed circle radius a, we have

$$r_s(\theta) = \frac{a}{\cos\theta}, \theta \in \left[-\frac{\pi}{4}, \frac{\pi}{4}\right], \tag{A1}$$

$$p_s(\theta) = \frac{r_s(\theta)^2/2}{4\int_{-\frac{\pi}{4}}^{\frac{\pi}{4}} (r_s(\theta)^2/2)\mathrm{d}\theta} = \frac{\frac{a^2}{2\cos^2\theta}}{4a^2} = \frac{1}{8\cos^2\theta}, \tag{A2}$$

$$S = -4\int_{-\frac{\pi}{4}}^{\frac{\pi}{4}} p_s \log(p_s)\mathrm{d}\theta = 1.81549\ldots \tag{A3}$$

For a regular pentagon with an inscribed circle radius a, we have

$$r_s(\theta) = \frac{a}{\cos\theta}, \theta \in \left[-\frac{\pi}{5}, \frac{\pi}{5}\right], \tag{A4}$$

$$p_s(\theta) = \frac{r_s(\theta)^2/2}{5\int_{-\frac{\pi}{5}}^{\frac{\pi}{5}}(r_s(\theta)^2/2)\mathrm{d}\theta} = \frac{\frac{a^2}{2\cos^2\theta}}{5\times 2\sqrt{5-2\sqrt{5}}a^2}, \tag{A5}$$

$$S = -5\int_{-\frac{\pi}{5}}^{\frac{\pi}{5}} p_s \log(p_s)\mathrm{d}\theta = 1.82964\ldots \tag{A6}$$

For a regular hexagon with an inscribed circle radius a, we have

$$r_s(\theta) = \frac{a}{\cos\theta}, \theta \in \left[-\frac{\pi}{6}, \frac{\pi}{6}\right], \tag{A7}$$

$$p_s(\theta) = \frac{r_s(\theta)^2/2}{6\int_{-\frac{\pi}{6}}^{\frac{\pi}{6}}(r_s(\theta)^2/2)\mathrm{d}\theta} = \frac{\frac{a^2}{2\cos^2\theta}}{4\sqrt{3}a^2} = \frac{1}{8\sqrt{3}\cos^2\theta}, \tag{A8}$$

$$S = -6\int_{-\frac{\pi}{6}}^{\frac{\pi}{6}} p_s \log(p_s)\mathrm{d}\theta = 1.83412\ldots \tag{A9}$$

References

1. Zhang, Y.; Michel, P. Shapes, structures, and evolution of small bodies. *Astrodyn* **2021**, *5*, 293–329. [CrossRef]
2. IAU2006 General Assembly. Resolution B5: Definition of a Planet in the Solar System. Available online: https://www.iau.org/static/resolutions/Resolution_GA26-5-6.pdf (accessed on 9 December 2022).
3. Spohn, T. Small Solar System Body. In *Encyclopedia of Astrobiology*; Gargaud, M., Irvine, W.M., Amils, R., James, H., Pinti, D.L., Quintanilla, J.C., Rouan, D., Spohn, T., Tirard, S., Viso, M., Eds.; Springer: Berlin/Heidelberg, Germany, 2011; pp. 1516–1517. [CrossRef]
4. Sugiura, K.; Kobayashi, H.; Inutsuka, S. Toward understanding the origin of asteroid geometries-variety in shapes produced by equal-mass impacts. *Astron. Astrophys.* **2018**, *620*, A167. [CrossRef]
5. Yu, Y.; Baoyin, H. Orbital dynamics in the vicinity of asteroid 216 Kleopatra. *Astron. J.* **2012**, *143*, 62. [CrossRef]
6. Jiang, Y.; Baoyin, H.; Wang, X.; Yu, Y.; Li, H.; Peng, C.; Zhang, Z. Order and chaos near equilibrium points in the potential of rotating highly irregular-shaped celestial bodies. *Nonlinear Dyn.* **2016**, *83*, 231–252. [CrossRef]
7. Wang, X.; Jiang, Y.; Gong, S. Analysis of the Potential Field and Equilibrium Points of Irregular-shaped Minor Celestial Bodies. *Astrophys. Space Sci.* **2014**, *353*, 105–121. [CrossRef]
8. Yu, Y.; Baoyin, H. Generating families of 3D periodic orbits about asteroids. *Mon. Not. R. Astron. Soc.* **2012**, *427*, 872–881. [CrossRef]
9. Yu, Y.; Baoyin, H.; Jiang, Y. Constructing the natural families of periodic orbits near irregular bodies. *Mon. Not. R. Astron. Soc.* **2015**, *453*, 3269–3277. [CrossRef]
10. Jiang, Y.; Yu, Y.; Baoyin, H. Topological classifications and bifurcations of periodic orbits in the potential field of highly irregular-shaped celestial bodies. *Nonlinear Dyn.* **2015**, *81*, 119–140. [CrossRef]
11. Jiang, Y.; Baoyin, H.; Li, H. Periodic motion near the surface of asteroids. *Astrophys. Space Sci.* **2015**, *360*, 63. [CrossRef]
12. Ni, Y.; Jiang, Y.; Baoyin, H. Multiple bifurcations in the periodic orbit around Eros. *Astrophys. Space Sci.* **2016**, *361*, 170. [CrossRef]
13. Lan, L.; Ni, Y.; Jiang, Y.; Li, J. Motion of the moonlet in the binary system 243 Ida. *Acta Mech. Sin.* **2018**, *34*, 214–224. [CrossRef]
14. Gil-Fernandez, J.; Ortega-Hernando, G. Autonomous vision-based navigation for proximity operations around binary asteroids. *CEAS Space J.* **2018**, *10*, 287–294. [CrossRef]
15. Pellacani, A.; Cabral, F.; Alcalde, A.; Kicman, P.; Lisowski, J.; Gerth, I.; Burmann, B. Semi-autonomous attitude guidance using relative navigation based on line of sight measurements: Aim scenario. *Acta Astronaut.* **2018**, *152*, 496–508. [CrossRef]
16. Hu, W.; Scheeres, D.J. Numerical determination of stability regions for orbital motion in uniformly rotating second degree and order gravity fields. *Planet. Space Sci.* **2004**, *52*, 685–692. [CrossRef]
17. Scheeres, D.J.; Ostro, S.J.; Hudson, R.S.; Werner, R.A. Orbits close to asteroid 4769 Castalia. *Icarus* **1996**, *121*, 67–87. [CrossRef]
18. de Pater, I.; Lissauer, J.J. *Planetary Sciences*, 2nd ed.; Cambridge University Press: Cambridge, UK, 2015; pp. 247–248. [CrossRef]
19. Zhuravlev, S.G. Stability of the libration points of a rotating triaxial ellipsoid. *Celest. Mech.* **1972**, *6*, 255–267. [CrossRef]

20. Scheeres, D.J. Dynamics about uniformly rotating triaxial ellipsoids: Applications to asteroids. *Icarus* **1994**, *110*, 225–238. [CrossRef]
21. Jiang, Y. Equilibrium points and periodic orbits in the vicinity of asteroids with an application to 216 Kleopatra. *Earth Moon Planets* **2015**, *115*, 31–44. [CrossRef]
22. Jiang, Y.; Ni, Y.; Baoyin, H.; Li, J.; Liu, Y. Asteroids and Their Mathematical Methods. *Mathematics* **2022**, *10*, 2897. [CrossRef]
23. Riaguas, A.; Elipe, A.; López-Moratalla, T. Non-Linear Stability of the Equilibria in the Gravity Field of a Finite Straight Segment. *Celest. Mech. Dyn. Astron.* **2001**, *81*, 235–248. [CrossRef]
24. Broucke, R.; Elipe, A. The Dynamics of Orbits in a Potential Field of a Solid Circular Ring. *Regul. Chaotic Dyn.* **2005**, *10*, 129–143. [CrossRef]
25. Romanov, V.A.; Doedel, E.J. Periodic Orbits Associated with the Libration Points of the Homogeneous Rotating Gravitating Triaxial Ellipsoid. *Int. J. Bifurc. Chaos* **2012**, *22*, 1230035. [CrossRef]
26. Zeng, X.; Jiang, F.; Li, J.; Baoyin, H. Study on the Connection between the Rotating Mass Dipole and Natural Elongated Bodies. *Astrophys. Space Sci.* **2015**, *356*, 29–42. [CrossRef]
27. Zhang, Y.; Qian, Y.; Li, X.; Yang, X. Resonant orbit search and stability analysis for elongated asteroids. *Astrodynamics* **2023**, *7*, 51–67. [CrossRef]
28. Miller, J.K.; Konopliv, A.S.; Antreasian, P.G.; Bordi, J.J.; Chesley, S.; Helfrich, C.E.; Scheeres, D.J.; Owen, W.M.; Wang, T.C.; Williams, B.G.; et al. Determination of Shape, Gravity, and Rotational State of Asteroid 433 Eros. *Icarus* **2002**, *155*, 3–17. [CrossRef]
29. Takahashi, Y.; Bradley, N.; Kennedy, B. Determination of Celestial Body Principal Axes via Gravity Field Estimation. *J. Guid. Control Dyn.* **2017**, *40*, 3050–3060. [CrossRef]
30. Romain, G.; Jean-Pierre, B. Ellipsoidal Harmonic Expansions of the Gravitational Potential: Theory and Application. *Celest. Mech. Dyn. Astron.* **2001**, *79*, 235–275. [CrossRef]
31. Rossi, A.; Marzari, F.; Farinella, P. Orbital Evolution around Irregular Bodies. *Earth Planets Space* **1999**, *51*, 1173–1180. [CrossRef]
32. Dechambre, D.; Scheeres, D.J. Transformation of Spherical Harmonic Coefficients to Ellipsoidal Harmonic Coefficients. *Astron. Astrophys.* **2002**, *387*, 1114–1122. [CrossRef]
33. Garmier, R.; Barriot, J.P.; Konopliv, A.S.; Yeomans, D.K. Modeling of the Eros gravity Field as an Ellipsoidal Harmonic Expansion from the NEAR Doppler Tracking Data. *Geophys. Res. Lett.* **2002**, *29*, 721–723. [CrossRef]
34. Geissler, P.; Petit, J.M.; Durda, D.D.; Greenberg, R.; Bottke, W.; Nolan, M.; Moore, J. Erosion and Ejecta Reaccretion on 243 Ida and Its Moon. *Icarus* **1996**, *120*, 140–157. [CrossRef]
35. Werner, R.A. The Gravitational Potential of a Homogeneous Polyhedron or Don't Cut Corners. *Celest. Mech. Dyn. Astron.* **1994**, *59*, 253–278. [CrossRef]
36. Werner, R.A. *On the Gravity Field of Irregularly Shaped Celestial Bodies*; The University of Texas at Austin: Austin, TX, USA, 1996.
37. Werner, R.A.; Scheeres, D.J. Exterior Gravitation of a Polyhedron Derived and Compared with Harmonic and Mascon Gravitation Representations of Asteroid 4769 Castalia. *Celest. Mech. Dyn. Astron.* **1996**, *65*, 313–344. [CrossRef]
38. Mirtich, B. Fast and Accurate Computation of Polyhedral Mass Properties. *J. Graph. Tools* **1996**, *1*, 31–50. [CrossRef]
39. Zhang, Y.; Yu, Y.; Baoyin, H. Dynamical behavior of flexible net spacecraft for landing on asteroid. *Astrodynamics* **2021**, *5*, 249–261. [CrossRef]
40. Zhao, Y.; Yang, H.; Hu, J. The Fast Generation of the Reachable Domain for Collision-Free Asteroid Landing. *Mathematics* **2022**, *10*, 3763. [CrossRef]
41. Li, X.; Scheeres, D.J.; Qiao, D.; Liu, Z. Geophysical and orbital environments of asteroid 469219 2016 HO3. *Astrodyn.* **2023**, *7*, 31–50. [CrossRef]
42. Oki, Y.; Yoshikawa, K.; Takeuchi, H.; Kikuchi, S.; Ikeda, H.; Scheeres, D.J.; McMahon, J.W.; Kawaguchi, J.; Takei, Y.; Mimasu, Y.; et al. Orbit insertion strategy of Hayabusa2's rover with large release uncertainty around the asteroid Ryugu. *Astrodyn* **2020**, *4*, 309–329. [CrossRef]
43. Buonagura, C.; Pugliatti, M.; Topputo, F. Image Processing Robustness Assessment of Small-Body Shapes. *J. Astronaut. Sci.* **2022**, *69*, 1744–1765. [CrossRef]
44. Ni, Y.; Turitsyn, K.; Baoyin, H.; Li, J. Entropy Method of Measuring and Evaluating Periodicity of Quasi-periodic Trajectories. *Sci. China Phys. Mech. Astron.* **2018**, *61*, 064511. [CrossRef]
45. Neese, C.E. Small Body Radar Shape Models V2.0. EAR-A-5-DDRRADARSHAPE-MODELS-V2.0, NASA Planetary Data System. 2004. Available online: https://data.nasa.gov/Earth-Science/SMALL-BODY-RADAR-SHAPE-MODELS-V2-0/qckk-73zc (accessed on 9 December 2022).